



**The Role of Excited-State Topology in Three-Body
Dissociation of sym-Triazine**

John D. Savee, *et al.*
Science **321**, 826 (2008);
DOI: 10.1126/science.1157617

***The following resources related to this article are available online at
www.sciencemag.org (this information is current as of November 20, 2008):***

Updated information and services, including high-resolution figures, can be found in the online version of this article at:

<http://www.sciencemag.org/cgi/content/full/321/5890/826>

Supporting Online Material can be found at:

<http://www.sciencemag.org/cgi/content/full/321/5890/826/DC1>

This article appears in the following **subject collections**:

Chemistry

<http://www.sciencemag.org/cgi/collection/chemistry>

Information about obtaining **reprints** of this article or about obtaining **permission to reproduce this article** in whole or in part can be found at:

<http://www.sciencemag.org/about/permissions.dtl>

summarized in Fig. 3A (right) and detailed in fig. S10. In each case, AFM imaging reveals the formation of long tubes (Fig. 4A), and AFM width measurement of randomly selected, opened tubes confirms the expected circumference monodispersity (Fig. 4A, insets, AFM images; Fig. 4B, a summary. See fig. S13 for details.) The length of SST tubes was investigated by using fluorescence microscopy (Fig. 4C). For seven-helix tubes, the average length is $\sim 6 \mu\text{m}$, with some tubes reaching $\sim 20 \mu\text{m}$.

Thermal formation and melting profiles of SST tubes (Fig. 4D) and SST ribbons (fig. S15) reveal hysteresis. Such hysteresis has also been observed in DNA lattices formed from multi-stranded tiles (27, 26). It is also worth noting that the annealing and melting curves of SST tubes and ribbons demonstrate only one sharp transition temperature. This is consistent with the expectation that single-stranded DNA oligonucleotides are directly assembled into the growing lattice during annealing and disassembled from the lattice during melting. In contrast, two or more characteristic transition temperatures are commonly observed in lattices based on multistranded rigid tiles (26, 27); the lowest temperature corresponds to lattice formation or melting, and the others correspond to tile formation or melting.

We suggest that the structural flexibility of SST may contribute to the success of the putative kinetic trapping of monodisperse tubes. The long sticky ends of SST and the flexible interhelix single-stranded linkage points in the assembled lattice may facilitate fast cyclization and hence trapping of the tubes with the smallest compatible number of helices. In addition, it is conceivable that in a nucleation-elongation model (26) (see fig. S16 for a hypothetical assembly pathway), the nucleation barrier difference between the k -helix tube and the $2k$ -helix tube may help trap the system into monodisperse k -helix tubes. The observed hysteresis (Fig. 4D) suggests the existence of a significant kinetic barrier during tube formation, and it is conceivable that this kinetic barrier is due to the presence of a nucleation barrier. It would be interesting to experimentally elucidate the kinetic assembly pathways of SST tubes. It would also be interesting to test if a similar kinetic strategy can be applied to programming the circumferences of DNA tubes assembled from multistranded rigid DNA tiles (9–15).

The ribbon and tube systems constructed here are likely to find applications ranging from biophysics to electronics and to nanotechnology. In biophysics, the programmable dimensions of the ribbons and tubes and, hence, their programmable physical properties, e.g., persistence length, make them attractive synthetic model systems. In electronics, metalization of DNA nanotubes (9, 11, 17) may result in nanowires with controlled diameters and, hence, controlled electronic properties. In nanotechnology, DNA nanotubes with programmable geometrical and mechanical properties can be used as building blocks for more sophisticated architectures and devices [e.g.,

tracks for molecular motors (28, 24, 3)] and as templates for organization of functional groups (9, 8).

References and Notes

- N. C. Seeman, *Nature* **421**, 427 (2003).
- U. Feldkamp, C. M. Niemeyer, *Angew. Chem. Int. Ed.* **45**, 1856 (2006).
- J. Bath, A. J. Turberfield, *Nat. Nanotechnol.* **2**, 275 (2007).
- N. C. Seeman, *Mol. Biotechnol.* **37**, 246 (2007).
- N. C. Seeman *et al.*, *Nanotechnology* **9**, 257 (1998).
- T. J. Fu, N. C. Seeman, *Biochemistry* **32**, 3211 (1993).
- E. Winfree, F. Liu, L. A. Wenzler, N. C. Seeman, *Nature* **394**, 539 (1998).
- C. Lin, Y. Liu, S. Rinker, H. Yan, *ChemPhysChem* **7**, 1641 (2006).
- H. Yan, S. H. Park, G. Finkelstein, J. H. Reif, T. H. LaBean, *Science* **301**, 1882 (2003).
- J. C. Mitchell, J. R. Harris, J. Malo, J. Bath, A. J. Turberfield, *J. Am. Chem. Soc.* **126**, 16342 (2004).
- D. Liu, S. H. Park, J. H. Reif, T. H. LaBean, *Proc. Natl. Acad. Sci. U.S.A.* **101**, 717 (2004).
- P. W. K. Rothmund *et al.*, *J. Am. Chem. Soc.* **126**, 16344 (2004).
- D. Reishus, B. Shaw, Y. Brun, N. Chelyapov, L. Adleman, *J. Am. Chem. Soc.* **127**, 17590 (2005).
- H. Liu, Y. Chen, Y. He, A. E. Ribbe, C. Mao, *Angew. Chem. Int. Ed.* **45**, 1942 (2006).
- Y. Ke, Y. Liu, J. Zhang, H. Yan, *J. Am. Chem. Soc.* **128**, 4414 (2006).
- F. Mathieu *et al.*, *Nano Lett.* **5**, 661 (2005).
- S. H. Park *et al.*, *Nano Lett.* **5**, 693 (2005).
- B. Wei, Y. Mi, *Biomacromolecules* **6**, 2528 (2005).
- W. B. Sherman, N. C. Seeman, *Biophys. J.* **90**, 4546 (2006).
- S. M. Douglas, J. J. Chou, W. M. Shih, *Proc. Natl. Acad. Sci. U.S.A.* **104**, 6644 (2007).
- A. Kuzuya, R. Wang, R. Sha, N. C. Seeman, *Nano Lett.* **7**, 1757 (2007).
- The half-crossover can be viewed as a simplified Holliday-junction analog, which utilizes one strand, rather than the normal two strands, at the crossover

exchange point. A similar structure was previously used in constructing DNA nanotubes (24).

- Due to the modularity and standardization of the motif, assigning the dimensions of all the green domains in the lattice also uniquely determines the dimensions of all the other domains.
- P. Yin, H. M. T. Choi, C. R. Calvert, N. A. Pierce, *Nature* **451**, 318 (2008).
- Materials and methods are available as supporting material on Science Online.
- R. Schulman, E. Winfree, *Proc. Natl. Acad. Sci. U.S.A.* **104**, 15236 (2007).
- R. D. Barish, P. W. K. Rothmund, E. Winfree, *Nano Lett.* **5**, 2586 (2005).
- R. Pei *et al.*, *J. Am. Chem. Soc.* **128**, 12693 (2006).
- The authors thank E. Winfree at Caltech for generously hosting the majority part of this work in his lab. For inspiring discussions, the authors thank E. Winfree, P. W. K. Rothmund, R. Schulman, V. A. Beck, J. R. Viereg, R. D. Barish, B. Yurke, D. Y. Zhang, N. A. Pierce, S. Hamada, M. Bockrath, H. Maune, Y. Huang, C. R. Calvert, N. L. Dabby, and J. Kim. The authors are also grateful to N. A. Pierce at Caltech and J. Liu at Duke for facility support, to the Pierce group for the use of the unpublished DNA sequence design component and DNA structure illustration component of the NUPACK server (www.nupack.org), and to B. Walters for technical assistance. The fluorescence microscope was built by R.F.H. and B. Yurke. There is a patent pending on this work. This work is supported by the Center for Biological Circuit Design at Caltech, NSF grants CCF-0523555 and CCF-0432038 to J.H.R., NSF grant CBET-0508284 to T.H.L., NSF grants 0622254 and 0432193 to E. Winfree, and NSF grant 0506468 to N. A. Pierce.

Supporting Online Material

www.sciencemag.org/cgi/content/full/321/5890/824/DC1
Materials and Methods
Texts S1 and S2
Figs. S1 to S16

4 March 2008; accepted 16 June 2008
10.1126/science.1157312

The Role of Excited-State Topology in Three-Body Dissociation of *sym*-Triazine

John D. Savee,¹ Vadim A. Mozhayskiy,² Jennifer E. Mann,¹
Anna I. Krylov,^{2*} Robert E. Continetti^{1*}

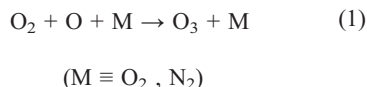
Molecular fragmentation into three products poses an analytical challenge to theory and experiment alike. We used translational spectroscopy and high-level ab initio calculations to explore the highly debated three-body dissociation of *sym*-triazine to three hydrogen cyanide molecules. Dissociation was induced by charge exchange between the *sym*-triazine radical cation and cesium. Calculated state energies and electronic couplings suggest that reduction initially produces a population of *sym*-triazine partitioned between the 3s Rydberg and $\pi^* \leftarrow n$ electronically excited manifolds. Analysis of the topology of these manifolds, along with momentum correlation in the dissociation products, suggests that a conical intersection of two potential energy surfaces in the 3s Rydberg manifold leads to stepwise dissociation, whereas a four-fold glancing intersection in the $\pi^* \leftarrow n$ manifold leads to a symmetric concerted reaction.

Molecular dissociation plays an important role in the chemistry of nonequilibrium environments where sufficient energy is available to break a chemical bond. Most photoinitiated dissociation processes in the lower layers of Earth's atmosphere are two-body

processes, for which dynamical information can be obtained through relatively straightforward experiments. However, in combustion processes, the stratosphere, interstellar space, and other lower-density environments, high-energy processes (e.g., dissociative recombination) can read-

ily induce three-body dissociation of neutral molecules. Because of the inherent difficulties in predicting nonadiabatic behavior of excited molecules and in directly observing multiple dissociation products, the acquisition of dynamical information for three-body processes has proven to be a challenge for theoreticians and experimentalists alike.

For many of the systems for which dynamical information is available, there is a history of controversy over whether the dissociation proceeds in a stepwise or a concerted fashion (1). The mechanistic controversy stems from the challenges of characterizing dissociation of a polyatomic system at a molecular level. Several of the reactions are believed to proceed through symmetric transition states and involve truly simultaneous (i.e., within one rotational period) breaking of two bonds. Moreover, the reverse reaction is a termolecular association reaction and is generally improbable on account of collision statistics (2). Yet termolecular reactions are important; a prominent example is ozone formation, where a three-body reactive collision is an essential part of the mechanism (3):



sym-Triazine (Tz) is among the largest molecules known to undergo photoinduced three-body decay. Because of the relative stability of hydrogen cyanide (HCN), three-body dissociation of Tz exhibits the interesting property of producing three identical molecular products:



This unique feature has stirred a mechanistic controversy from past experiments where dynamical information consisted of ensemble averages rather than discrete measurement of momentum partitioning to each HCN fragment per event (4–8). In these translational spectroscopy experiments (4, 5), dissociation was believed to be initiated by photoexcitation to the $\pi^* \leftarrow n$ and $\pi^* \leftarrow \pi$ electronically excited manifolds, although dissociation to 3HCN occurs ultimately through decay to the ground state, as dictated by symmetry correlation arguments and energy balance (9). The original study by Ondrey and Bersohn assumed that the three HCN photo-products were produced in concerted fashion and therefore received an equal momentum partitioning (4). However, a later study by Gejo *et al.* presented evidence in favor of stepwise dissoci-

ation (5). Ab initio calculations of transition states along with classical trajectory studies have found that the barrier to a symmetric concerted reaction lies lowest in energy, but suggest that at higher excitation energies the stepwise mechanism could become more prevalent (6–8).

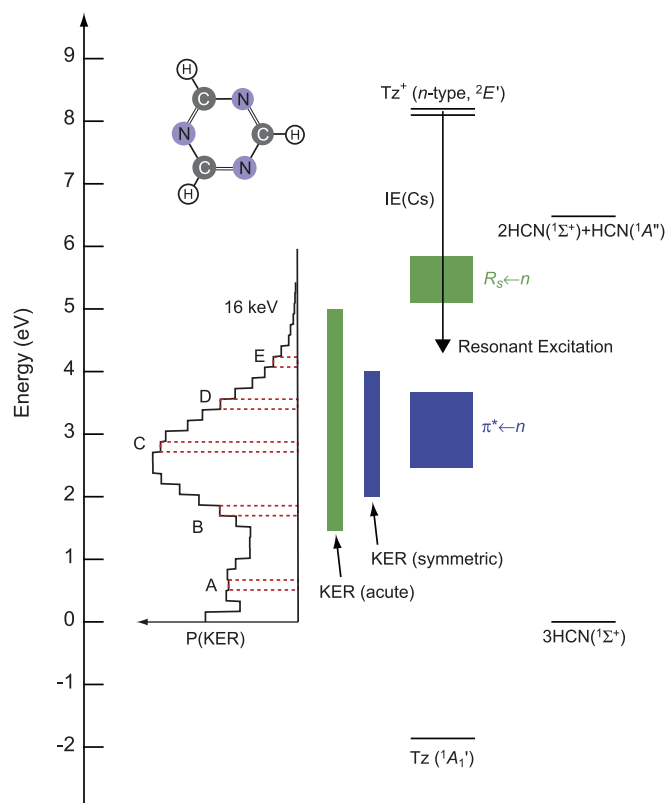
Here, we report translational spectroscopy of the three-body dissociation of Tz by means of coincidence detection techniques (10, 11). Unlike time-of-flight techniques, which forced numerous assumptions in the previous studies, coincidence detection methods provide a complete kinematic characterization of the dissociation process. Because coincidence experiments of this nature require a fast neutral beam, Tz was excited via charge exchange (CE) between a keV Tz cation (Tz^+) beam and an alkali electron donor, cesium (Cs) (12, 13). The production of excited neutral molecules by CE has been well studied (13–15), and recent studies of the CE-induced three-body dissociation of H_3 have confirmed the utility of coincidence techniques for investigating dissociation dynamics (16, 17). The complex electronic structure of Tz and the intricate mechanism by which CE deposits energy in the neutral acceptor prompted a concurrent investigation using state-of-the-art ab initio methods, which proved instrumental in the interpretation of our experimental observations.

Figure 1 shows the measured kinetic energy release distribution, $\text{P}(\text{KER})$, for the HCN fragments produced by CE-induced dissociation of Tz with a 16-keV Tz^+ beam, accompanied by relevant dissociation limits, calculated electronic-

state minima, and energy thresholds. $\text{P}(\text{KER})$ distributions obtained at 12 and 16 keV are similar and extend from 0 to 5 eV, with a major feature peaked at 2.6 eV, a minor feature at 0.5 eV, and a maximum KER at ~ 5 eV. To illustrate the KER-dependent dissociation dynamics, we divided the $\text{P}(\text{KER})$ distribution into 32 bins and then used Dalitz representations (18) to visualize the momentum partitioning among the fragments for the events contained within each bin. Several Dalitz representations constructed from the 12- and 16-keV Tz data are shown in Fig. 2, corresponding to the labeled KER ranges in Fig. 1. An “acute” feature (two slow HCN fragments and one fast HCN fragment) dominates the Dalitz representations between intervals B and E at both beam energies. A symmetric feature (equal momentum partitioning) is also present alongside the acute feature for intervals C and D at both beam energies, although it is more apparent in the 16-keV Dalitz plots. Evaluation of Dalitz plots over the full KER range reveals that the acute feature spans 1.5 to 5 eV, whereas the symmetric feature is confined in the 2- to 4-eV range (denoted in Fig. 1).

It is apparent that we have observed two unique dissociation mechanisms, one with symmetric and another with asymmetric momentum partitioning. The former is consistent with a concerted mechanism for the three-body breakup, whereas we found the latter to be consistent with stepwise decomposition (11). We found that the ratio of symmetric to asymmetric Dalitz features depends on the beam energy, which suggests that

Fig. 1. Energy diagram for the three-body dissociation of Tz. The $\text{P}(\text{KER})$ distribution obtained with a 16-keV cation beam is shown on the left. Labeled KER intervals correspond to the following energies: A, 0.51 to 0.68 eV; B, 1.69 to 1.86 eV; C, 2.70 to 2.87 eV; D, 3.38 to 3.54 eV; E, 4.05 to 4.22 eV. The colored boxes labeled “KER (acute)” and “KER (symmetric)” mark the region over which the mechanism was observed. The colored boxes labeled “3s Rydberg” and “ $\pi^* \leftarrow n$ ” denote the regions between the lowest- and highest-lying states (triplets included) in each manifold, as computed at the cation equilibrium geometry (C_{2v}). Zero energy corresponds to the ground-state energy of 3HCN.



¹Department of Chemistry and Biochemistry, University of California, San Diego, La Jolla, CA 92093, USA. ²Department of Chemistry, University of Southern California, Los Angeles, CA 90089, USA.

*To whom correspondence should be addressed. E-mail: krylov@usc.edu (A.I.K.); rcontinetti@ucsd.edu (R.E.C.).

different excited states are populated and consequently decay via different mechanisms.

Electronic structure calculations of Tz and $(\text{Cs-Tz})^+$ were used to characterize the potential energy surfaces (PESs) of the relevant electronic states, as well as electronic couplings that control the CE process, allowing us to identify the gateway states for the symmetric and asymmetric dissociation and to explain the observed trends. The extremely dense electronic spectrum of Tz and extensive degeneracies (19–21) posed unique challenges for theory, which we were able to address by judicious choice of appropriate equation-of-motion coupled-cluster (EOM-CC) models (22–24) combining high ac-

curacy with a balanced description of multiple states (11).

CE between keV cation beams and alkali electron donors has been shown to potentially populate multiple states in the resulting neutral species. Identifying the initially populated states that give rise to the two distinct mechanisms is a daunting task for ab initio calculations in view of the dense electronic spectrum of Tz, which consists of manifolds of valence $\pi^* \leftarrow \pi$ and $\pi^* \leftarrow n$ states (19–21), along with Rydberg states derived from the transitions from nitrogen lone pairs (n) and π orbitals. Our calculations (11) identified >20 states of neutral Tz below 9 eV. Energetically, CE is expected to excite Tz resonantly (i.e., at the difference between ionization energies of Tz and Cs, which are 10.01 and 3.89 eV, respectively) 6.12 eV above its ground state (19). However, nonresonant processes can occur when a strong perturbation acts on a zero-order system (e.g., noninteracting Cs and Tz^+) for a relatively short time, as in energetic collisions or in intense laser fields. In the context of CE, the Demkov model (11) demonstrates mathematically how short interacting times (i.e.,

large velocities) give rise to increased probability for populating nonresonant states. The total energy is conserved by redistribution of the electronic energy among internal and translational degrees of freedom of the system.

Examination of the energy diagram in Fig. 1 and computed excitation energies (11) reveals several singlet and triplet states that are energetically accessible according to the observed KER range (e.g., all of the $\pi^* \leftarrow n$ and $\pi^* \leftarrow \pi$ states, as well as the lowest Rydberg $R_s \leftarrow n$ state). By considering several characteristics of the excited states—their excitation energies, nonadiabatic couplings, and the topologies of the corresponding Jahn-Teller (JT) manifolds—we were able to identify the most likely initially populated states as the A_1 3s Rydberg and the A_2 $\pi^* \leftarrow n$ valence states, as follows.

To discriminate between the different states, we used a simple Demkov two-state model to evaluate transition probabilities for the CE process (25). The transition probability derived from this model depends on the potential energy difference (i.e., the off-resonant energy defect), the potential parameter in the coupling

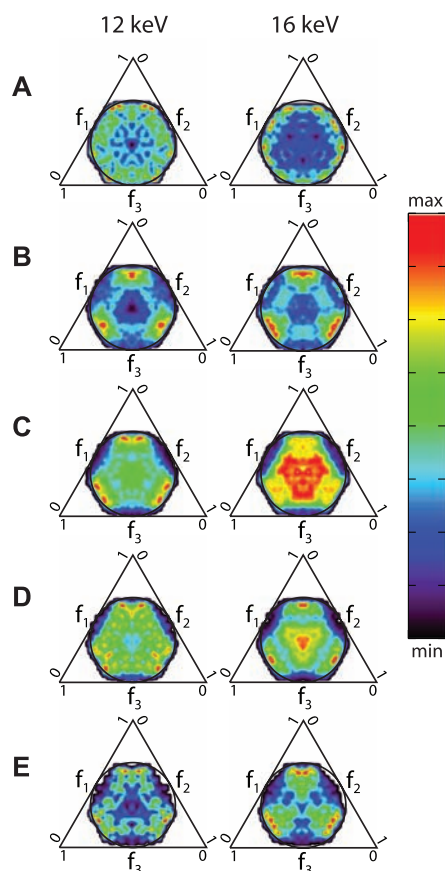


Fig. 2. Dalitz representations of the momentum correlation in the three-body breakup of Tz obtained over the KER intervals (A to E) denoted in Fig. 1. The Dalitz plot is a histogram with each of the three axes corresponding to the fractional square (f_i) of the momentum (p_i) partitioned to a particular HCN fragment ($f_i = p_i^2 / \sum p_i^2$), and each point within the circular region of momentum conservation represents a particular arrangement of the three momentum vectors giving rise to a single event. For example, the symmetric partitioning of the momentum yields the intensity in the center of the Dalitz plots, whereas the intensity near the apexes (i.e., acute features) corresponds to one fast and two slow fragments. The Dalitz plots have been slightly cropped near the intense acute apexes to illustrate the dynamic change in other regions of the plots.

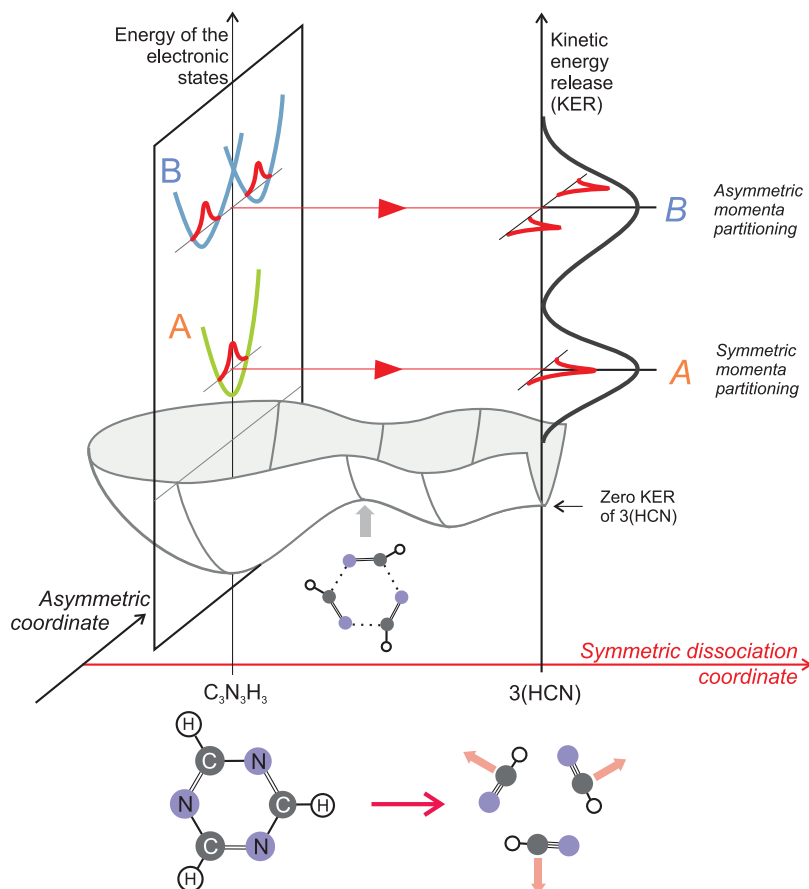


Fig. 3. Two-dimensional representation of the ground-state and excited-state PESs, demonstrating mapping of the initial wave function into the product distribution (i.e., the reflection principle). The two coordinates are the reaction coordinate for the three-body dissociation and a symmetry-lowering displacement (e.g., JT deformation). The reflection principle, which assumes ballistic dissociation on the lowest PES, predicts symmetric energy partitioning for the process initiated on the symmetric PES (right), and asymmetric partitioning for a JT distorted PES.

matrix element, and the relative velocity between the cation and the atomic electron donor (25). For a given interaction time determined by the atom-ion relative velocity, the model predicts a larger probability of populating states with a smaller energy defect (i.e., in resonance) and larger coupling. The velocity dependence of branching ratios between different channels is nonlinear and is determined chiefly by the energy defect. The relative probability of populating the state with a smaller energy defect (versus a larger defect) increases as the relative ion-atom velocity increases. Thus, the observed velocity-dependent change in relative intensity of the two Dalitz features qualitatively suggests that two different initial states of the neutral molecule give rise to the observed dissociation channels.

To evaluate the electronic couplings responsible for CE between Cs and Tz^+ , we used EOM-CC wave functions of the combined $(\text{Cs-Tz})^+$ system (11) in a generalized Mulliken-Hush (GMH) approach (26). The calculations show that couplings between Cs-Tz^+ and different Cs^+-Tz^* states are significant for the $\pi^* \leftarrow n$ and Rydberg states. Furthermore, the $\pi^* \leftarrow \pi$ couplings are nearly zero because of the two-electron character of the corresponding electronic transition (the ground state of Tz^+ has a hole in a lone pair orbital). The same arguments apply to the corresponding triplet states, which are accessible in CE experiments. The considerable electronic coupling matrix elements for the 3s Rydberg and $\pi^* \leftarrow n$ manifolds suggest these states as the most likely initially populated electronic states. However, the coupling for the Rydberg state is two orders of magnitude larger than that of the $\pi^* \leftarrow n$ state. Thus, the Demkov model predicts a much higher probability of populating the Rydberg state, even though it is farther off-resonance than is the $\pi^* \leftarrow n$ state. The respective equilibrium geometries of these states can therefore be considered as starting

points on the neutral ground-state surface by virtue of the reflection principle (Fig. 3).

A necessary condition for concerted dissociation is the existence of an appropriate energetically accessible transition state, and many theoretical studies of the interplay between concerted and stepwise mechanisms have focused on locating and comparing different transition states (2). Tz has an accessible symmetric transition state for three-body dissociation (8); however, a complete picture of the mechanism requires information about dynamics, which in turn depends on how the process was initiated. This aspect of the dynamics—the effect of initial conditions on the reaction outcome—can be understood within the reflection principle framework (27). In photodissociation, the reflection principle assumes a ballistic process (i.e., no vibrational equilibration) on the excited-state surface, which therefore acts as a mirror reflecting the initial wave packet onto the final product states. In the present experiment, the role of excited-state and ground-state surfaces is reversed: Tz is prepared in an electronically excited state, and dissociation occurs ultimately on the ground electronic state.

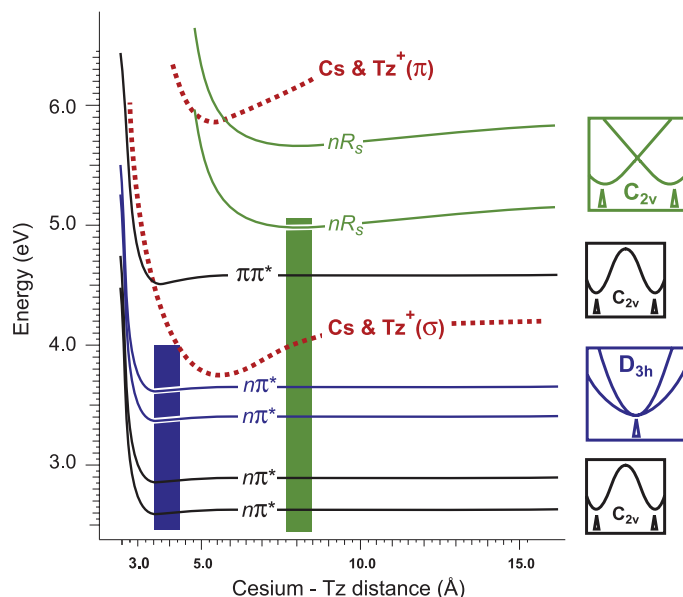
In the context of three-body breakup on the PES with a symmetric transition state, the reflection principle predicts symmetric momentum partitioning for the initially symmetric wave packet and asymmetric partitioning for the initial conditions described by the asymmetric wave packet (Fig. 3). The shape of the initial wave packet is determined by the shape of the corresponding excited-state surface on which Tz is produced by CE. Because all of the electronically excited states of Tz in the relevant energy region are derived by transitions between doubly degenerate orbitals, they are subject to asymmetric JT distortions. However, some of the states have a symmetric PES by virtue of the double degeneracy of both initial and target

molecular orbitals (MOs) and can therefore result in a symmetric wave packet (28, 29).

It is possible to determine which of the previously identified states have symmetric equilibrium structures and which are distorted, simply by analyzing symmetries and the electronic configurations of the corresponding wave functions, as in recent N_3^+ studies (28, 29). All of the states discussed above are derived from transitions involving degenerate MOs and are therefore subject to JT distortions. States derived from the transitions between degenerate and nondegenerate MOs ($e \otimes a \rightarrow E$) form a familiar “Mexican hat”-shaped PES. The pair of $R_s \leftarrow n$ Rydberg states in Tz and the ground state of Tz^+ are of this type (13). A qualitatively different type of intersection occurs for the $\pi^* \leftarrow n$ states derived from excitations between two degenerate MO pairs producing two exactly degenerate and two nearly degenerate states (i.e., $e \otimes e \rightarrow E + A + B$). It can be shown that all four states are scrambled around the intersection, and linear terms for the degenerate states are very small (28, 29). Consequently, the intersection appears to be glancing rather than conical. Although the minimum of the upper degenerate PES is not exactly at D_{3h} , a small-magnitude distortion (e.g., 0.001 Å and 10^{-4} eV in cyclic N_3^+) suggests a negligible effect on the corresponding nuclear wave functions, which therefore could be treated as derived from the symmetric PES.

Figure 4 shows a scan of the calculated PESs for Cs approaching Tz^+ in a direction perpendicular to the molecular plane. Dashed and solid curves correspond to the Cs-Tz^+ and Cs^+-Tz states, respectively. At infinite separation, the state ordering is exactly as in neutral Tz at the cation geometry. The pictograms on the right show the topology of each PES around D_{3h} . Note that the diffuse $R_s \leftarrow n$ states become perturbed by approaching Cs at 7 Å, whereas the PESs of the valence states remain flat up to about 3.5 Å. Analysis of the topology shows that among the states in the energy range corresponding to the symmetric dissociation, the only states with a symmetric equilibrium structure are the upper $\pi^* \leftarrow n$ states. It is therefore most likely that these states are responsible for the symmetric channel. This presents the possibility that previous experiments accessing the $\pi^* \leftarrow n$ electronic manifold were indeed observing a symmetric concerted dissociation mechanism, even though the manifold was accessed in a different manner. The asymmetric dissociation may occur via all other energetically accessible states; however, the most likely candidate is the lowest Rydberg $R_s \leftarrow n$ state for which the GMH coupling is largest. Thus, we conclude that acute and symmetric dissociation occur after initial excitation into the 3s Rydberg and $\pi^* \leftarrow n$ manifolds, respectively. This assignment is supported by qualitative agreement between the observed intensity of these channels and the GMH matrix coupling elements.

Fig. 4. Potential energy curves for the relevant singlet electronic states of the $(\text{Cs-Tz})^+$ system in a T-shaped configuration. The geometry of the Tz moiety is that of the cation. The pictograms on the right show the PES topology for each state. As in Fig. 1, the colored boxes denote KER regions for which symmetric and asymmetric dissociation was observed. Energies are relative to the ground-state energy of 3HCN.



The energetic locations of the 3s Rydberg and $\pi^* \leftarrow n$ manifolds in the cation Franck-Condon region correlate well with the KER range over which each Dalitz feature was observed (Fig. 4). The maximum observed KER of 5 eV associated with the acute feature is close to the vertical energy for the Rydberg states (i.e., 5.17 and 5.11 eV above the 3HCN limit for the singlet and triplet, respectively). The maximum observed KER of 4 eV for symmetric dissociation lies 0.33 eV higher in energy than the vertical energy of the highest $\pi^* \leftarrow n$ state, 1A_2 , which is located at 3.67 eV above the 3HCN limit and has D_{3h} equilibrium structure. The small separation between singlet and triplet states does not allow us to discriminate between these manifolds. However, the three-fold degeneracy of the triplets might lead one to expect triplets to be populated more frequently. On the other hand, the rate of electronic relaxation to the ground-state singlet PES is likely to be much slower for the triplets.

Nonadiabatic processes that span multiple electronic states are ubiquitous in the chemistry of energetic molecules and play a notable role in many types of natural phenomena (e.g., in biological, atmospheric, and combustion chemistry). The interactions between different electronic states are important even for reactions proceeding on a single PES, as reaction barriers can often be explained in terms of coupled diabatic states correlating with the reactants and the products. Our results show the progress being made toward analytical approaches to understanding the complexities of larger molecules.

In a broader context, this work raises a number of fundamental questions: How common is it for the equilibrium structure of an excited electronic state to determine the outcome of a reaction proceeding on another surface, and to what extent can the reflection principle be applied to polyatomic systems? With how much confidence can one rely on electronic couplings when considering the possible pathways of a nonadiabatic process? Would the difference between conical and glancing intersections manifest itself so prominently in molecules with lower symmetry? These questions all warrant future study. Our results show that synergism between theory and experiment can lead to greater understanding of how nonadiabatic behavior plays a role in these complicated systems.

References and Notes

1. C. Maul, K. H. Gericke, *Int. Rev. Phys. Chem.* **16**, 1 (1997).
2. Y. Osamura, H. F. Schaefer, M. Dupuis, W. A. Lester, *J. Chem. Phys.* **75**, 5828 (1981).
3. J. Guenther, D. Krankowsky, K. Mauersberger, *Chem. Phys. Lett.* **324**, 31 (2000).
4. G. S. Ondrey, R. Bersohn, *J. Chem. Phys.* **81**, 4517 (1984).
5. T. Gejo, J. A. Harrison, J. R. Huber, *J. Phys. Chem.* **100**, 13941 (1996).
6. Y. A. Dyakov *et al.*, *J. Phys. Chem. A* **111**, 9591 (2007).
7. J. Lee *et al.*, *Phys. Chem. Chem. Phys.* **6**, 945 (2004).
8. S. V. Pai, C. F. Chabalowski, B. M. Rice, *J. Phys. Chem.* **100**, 5681 (1996).
9. Y. Osamura, M. Unno, K. Hashimoto, *J. Am. Chem. Soc.* **109**, 1370 (1987).
10. R. E. Continetti, *Annu. Rev. Phys. Chem.* **52**, 165 (2001).
11. See supporting material on Science Online.
12. L. Kolaitis, D. M. Lubman, *Anal. Chem.* **58**, 1993 (1986).
13. H. Kato, K. Hirao, K. Yamashita, *J. Mol. Struct. (Theochem)* **88**, 265 (1982).
14. A. Salop, D. C. Lorents, J. R. Peterson, *J. Chem. Phys.* **54**, 1187 (1971).

15. V. Sidis, *J. Phys. Chem.* **93**, 8128 (1989).
16. C. M. Laperle, J. E. Mann, T. G. Clements, R. E. Continetti, *Phys. Rev. Lett.* **93**, 153202 (2004).
17. U. Galster, F. Baumgartner, U. Müller, H. Helm, M. Jungen, *Phys. Rev. A* **72**, 062506 (2005).
18. R. H. Dalitz, *Philos. Mag.* **44**, 1068 (1953).
19. C. Fridh, L. Asbrink, B. O. Jonsson, E. Lindholm, *Int. J. Mass Spectrom. Ion Phys.* **8**, 85 (1972).
20. K. K. Innes, I. G. Ross, W. R. Moomaw, *J. Mol. Spectrosc.* **132**, 492 (1988).
21. A. B. J. Parusel, G. Kohler, H. Nooijen, *J. Phys. Chem. A* **103**, 4056 (1999).
22. J. F. Stanton, R. J. Bartlett, *J. Chem. Phys.* **98**, 7029 (1993).
23. H. Koch, O. Christiansen, P. Jorgensen, J. Olsen, *Chem. Phys. Lett.* **244**, 75 (1995).
24. A. I. Krylov, *Annu. Rev. Phys. Chem.* **59**, 433 (2008).
25. Y. N. Demkov, *Sov. Phys. JETP* **18**, 138 (1964).
26. R. J. Cave, M. D. Newton, *Chem. Phys. Lett.* **249**, 15 (1996).
27. R. Schinke, *Photodissociation Dynamics* (Cambridge Univ. Press, Cambridge, 1993), pp. 109–133.
28. V. A. Mozhaykiy, D. Babikov, A. I. Krylov, *J. Chem. Phys.* **124**, 224309 (2006).
29. J. J. Dillon, D. R. Yarkony, *J. Chem. Phys.* **126**, 124113 (2007).
30. Supported by U.S. Air Force Office of Scientific Research grant FA9550-04-1-0035 (J.D.S., J.E.M., and R.E.C.) and NSF grant CHE-0616271 (V.M. and A.I.K.). This work was conducted under the auspices of the iOpenShell Center for Computational Studies of Electronic Structure and Spectroscopy of Open-Shell and Electronically Excited Species, supported by NSF through Chemistry Research Instrumentation and Facilities Cyberinfrastructure and Research Facilities Program (CRIF:CRF) grants CHE-0625419, CHE-0624602, and CHE-0625237.

Supporting Online Material

www.sciencemag.org/cgi/content/full/321/5/890/826/DC1
Materials and Methods
Figs. S1 to S10
Tables S1 to S5
References

11 March 2008; accepted 23 June 2008
10.1126/science.1157617

Phyllosilicate Diversity and Past Aqueous Activity Revealed at Mawrth Vallis, Mars

Janice L. Bishop,^{1*} Eldar Z. Noe Dobrea,² Nancy K. McKeown,³ Mario Parente,⁴ Bethany L. Ehlmann,⁵ Joseph R. Michalski,⁶ Ralph E. Milliken,² Francois Poulet,⁶ Gregg A. Swayze,⁷ John F. Mustard,⁵ Scott L. Murchie,⁸ Jean-Pierre Bibring⁶

Observations by the Mars Reconnaissance Orbiter/Compact Reconnaissance Imaging Spectrometer for Mars in the Mawrth Vallis region show several phyllosilicate species, indicating a wide range of past aqueous activity. Iron/magnesium (Fe/Mg)–smectite is observed in light-toned outcrops that probably formed via aqueous alteration of basalt of the ancient cratered terrain.

This unit is overlain by rocks rich in hydrated silica, montmorillonite, and kaolinite that may have formed via subsequent leaching of Fe and Mg through extended aqueous events or a change in aqueous chemistry. A spectral feature attributed to an Fe²⁺ phase is present in many locations in the Mawrth Vallis region at the transition from Fe/Mg–smectite to aluminum/silicon (Al/Si)–rich units. Fe²⁺-bearing materials in terrestrial sediments are typically associated with microorganisms or changes in pH or cations and could be explained here by hydrothermal activity. The stratigraphy of Fe/Mg–smectite overlain by a ferrous phase, hydrated silica, and then Al-phyllosilicates implies a complex aqueous history.

The Mawrth Vallis outflow channel (~25°N, 20°W) cuts through the ancient cratered Noachian highland terrain near the border with the lowlands. A variety of rocks are exposed

that reveal the early aqueous history of the planet. Indurated light-toned units with complex spatial and stratigraphic relations are overlain by a darker, more heavily cratered material. Erosion in many

locations exposes phyllosilicate-bearing outcrop within the light-toned rocks (1). Here we describe the specific clay minerals identified.

Hyperspectral images acquired by the Compact Reconnaissance Imaging Spectrometer for Mars (CRISM) (2, 3) exhibit a variety of signatures in the visible/near-infrared (VNIR: ~0.4 to 4 μm) that are attributed to phyllosilicates and are consistent with observations of this area made by the Observatoire pour la Minéralogie, l'Eau, les Glaces et l'Activité (OMEGA) instrument on Mars Express (3–5). OMEGA data revealed the presence of montmorillonite and nontronite based on Al-OH and Fe-OH absorption bands near 2.2 and 2.3 μm, respectively (4, 6). OMEGA data (Fig. 1) show Fe/Mg-phyllosilicates near the outflow channel and in a few other large outcrops observable at

¹SETI Institute and NASA Ames Research Center, Mountain View, CA 94043, USA. ²Jet Propulsion Laboratory, California Institute of Technology, Pasadena, CA 91109, USA. ³Department of Earth and Planetary Sciences, University of California Santa Cruz, Santa Cruz, CA 95064, USA. ⁴Department of Electrical Engineering, Stanford University, Stanford, CA 94305, USA. ⁵Department of Geological Sciences, Brown University, Providence, RI 02912, USA. ⁶Institut d'Astrophysique Spatiale, Orsay, 91405, France. ⁷U.S. Geological Survey, Denver, CO 80225, USA. ⁸Johns Hopkins University Applied Physics Laboratory, Laurel, MD 20723, USA.

*To whom correspondence should be addressed. E-mail: jlbishop@seti.org